



**HAL**  
open science

# High precision measurement of the $^{151}\text{Sm}$ beta decay by means of a metallic magnetic calorimeter

Karsten Kossert, Martin Loidl, Xavier Mougeot, Michael Paulsen, Philipp Ranitzsch, Matias Rodrigues

► **To cite this version:**

Karsten Kossert, Martin Loidl, Xavier Mougeot, Michael Paulsen, Philipp Ranitzsch, et al.. High precision measurement of the  $^{151}\text{Sm}$  beta decay by means of a metallic magnetic calorimeter. Applied Radiation and Isotopes, 2022, 185, pp.110237. 10.1016/j.apradiso.2022.110237 . cea-03662368

**HAL Id: cea-03662368**

**<https://cea.hal.science/cea-03662368>**

Submitted on 9 May 2022

**HAL** is a multi-disciplinary open access archive for the deposit and dissemination of scientific research documents, whether they are published or not. The documents may come from teaching and research institutions in France or abroad, or from public or private research centers.

L'archive ouverte pluridisciplinaire **HAL**, est destinée au dépôt et à la diffusion de documents scientifiques de niveau recherche, publiés ou non, émanant des établissements d'enseignement et de recherche français ou étrangers, des laboratoires publics ou privés.

# High precision measurement of the $^{151}\text{Sm}$ beta decay by means of a metallic magnetic calorimeter

Karsten Kossert<sup>\*1</sup>, Martin Loidl<sup>2</sup>, Xavier Mougeot<sup>2</sup>, Michael Paulsen<sup>1</sup>, Philipp Ranitzsch<sup>1</sup>,  
Matias Rodrigues<sup>2</sup>

<sup>1</sup> *Physikalisch-Technische Bundesanstalt (PTB), Bundesallee 100, 38116 Braunschweig, Germany*

<sup>2</sup> *Université Paris-Saclay, CEA, List, Laboratoire National Henri Becquerel (LNE-LNHB), F-91120  
Palaiseau, France*

## Abstract

The beta decay of  $^{151}\text{Sm}$  was measured by means of a metallic magnetic calorimeter. The measurement and subsequent analysis yielded a beta spectrum with an outstanding high-energy resolution of about 70 eV (FWHM) at 22 keV and a very low energy threshold well below 400 eV. The spectrum exhibited unexpectedly elevated beta emission probabilities at very low energy that we have not been able to reproduce in our theoretical study. The data analysis was thus scrutinized and an independent analysis of the same data set carried out. All new approaches have confirmed the previously found shape of the beta spectrum. The measured spectrum was compared to predictions from an advanced theoretical modeling that includes the atomic exchange effect, precise radiative corrections as well as the realistic nuclear structure that usually plays an important role in first forbidden non-unique transitions.

The measured spectrum was then carefully analyzed to determine the maximum beta energy, which was found to be  $Q = 76.430(68)$  keV. The dominant beta decay of  $^{151}\text{Sm}$  populates the ground state of  $^{151}\text{Eu}$ , and a weak beta branch populates the first excited state of  $^{151}\text{Eu}$ . From

---

\* Corresponding author:  
e-mail address: Karsten.Kossert@ptb.de

our measurements, the probabilities of these two branches were determined to be 99.31(11)% and 0.69(11)%, respectively.

**Key words:**  $^{151}\text{Sm}$ ; metallic magnetic calorimeter; beta minus decay; Kurie plot; beta spectrum shapes

## 1. Introduction

In several previous works it was demonstrated that measurements by means of metallic magnetic calorimeters (MMCs) of beta emitting radionuclides embedded in a  $4\pi$  absorber can yield high precision beta spectra (Rotzinger et al., 2008; Loidl et al. 2010; Loidl et al., 2014). Since such spectra are extremely important for radionuclide metrology, e.g., when using liquid scintillation counting (see, e.g., Kossert et al., 2011; Kossert and Mougeot, 2015), Čerenkov counting (Kossert et al., 2011; Kossert et al., 2014) or classical microcalorimetry (Collé, 2007), further beta spectra were measured within the scope of the EMPIR project MetroBeta (Loidl et al., 2019; Loidl et al., 2020). The measurement data obtained during this project for  $^{151}\text{Sm}$  are scrutinized in this work with the aim of determining the maximum beta energy and comparing the beta spectrum with state-of-the art theoretical calculations.

The decay scheme of  $^{151}\text{Sm}$  is shown in Figure 1. The decay comprises two beta branches, with the dominant transition leading to the ground state of  $^{151}\text{Eu}$ . The weaker beta branch leads to an excited level of  $^{151}\text{Eu}$ , and the energy of the subsequent gamma transition causes a shift of the respective beta spectrum by 21.541 keV when using a  $4\pi$  calorimetric method such as in our MMC measurement. A detailed analysis of the measured MMC spectrum carried out in this work yielded the decay probabilities of both beta transitions. This demonstrates that valuable and fundamental data can be obtained from MMC spectra. We consider this to be an important milestone towards a planned high precision measurement of the beta decay of  $^{129}\text{I}$ , which

represents one important objective of the new EMPIR project called PrimA-LTD. In the case of  $^{129}\text{I}$ , the dominant beta branch goes to an excited level of  $^{129}\text{Xe}$ . It is anticipated that the corresponding energy shift of this second forbidden non-unique beta spectrum will allow us to measure its spectrum with the highest precision at very low energies, as it is shifted far beyond the detector's energy threshold. The planned experiment will therefore be very valuable for benchmarking theoretical approaches.

A survey of the literature indicates that studies of the  $^{151}\text{Sm}$  beta decay are scarce. Achor et al. (1959) carried out measurements with a magnetic lens spectrometer and from a Kurie plot determined a maximum beta energy of 75.9(6) keV. The extracted beta spectrum shape was similar to that of an allowed transition, though this statement only holds for the high-energy part of the spectrum: a closer examination of the Kurie plot indicates that at low energy (approx. < 22 keV) the measured data deviate from a linear function.

Another beta spectrum measurement was presented by Bé et al. (2015) within the scope of a comprehensive study to determine the  $^{151}\text{Sm}$  half-life. The measurements were carried out with a passivated implanted planar silicon (PIPS) detector at LNHB. Again, the spectrum shape was found to be in accordance with that of an allowed transition, but the spectrum could only be determined at energies higher than approx. 15 keV.

According to the most recent atomic mass evaluation, AME2020 (Wang et al., 2021), the recommended maximum beta energy of  $^{151}\text{Sm}$  is 76.5(5) keV. We will demonstrate here that the MMC measurements yielded a reliable new result with a considerably lower uncertainty.

## 2. MMC measurements

The source used for the MMC measurement was prepared from a purified  $^{151}\text{Sm}$  solution. Gamma spectrometry measurements on aliquots of this solution have revealed the presence of impurities of  $^{154}\text{Eu}$  and  $^{155}\text{Eu}$  as described by Bé et al. (2015). They defined 1 April 2014 as the reference date and found the activity ratios of  $A(^{154}\text{Eu})/A(^{151}\text{Sm})$  and  $A(^{155}\text{Eu})/A(^{151}\text{Sm})$  to be

0.033(2)% and 0.011(1)%, respectively. Our MMC measurements were carried out in the period from 14 to 29 January 2019. Consequently, the impurity portions had fallen to  $A(^{154}\text{Eu})/A(^{151}\text{Sm})=0.023(2)\%$  and  $A(^{155}\text{Eu})/A(^{151}\text{Sm})=0.006(1)\%$ . Although both of these nuclides are beta emitters, at this activity level we consider the potential distortion of the measured  $^{151}\text{Sm}$  spectrum to be negligible. The presence of the nuclides does, however, at least partially explain the background observed beyond the endpoint of the  $^{151}\text{Sm}$  spectrum. None of the X-ray or gamma-ray lines of either of these nuclides, or any other impurities, were detectable in the MMC spectrum.

The actual source preparation as well as the MMC measurements performed for this work have been described in previous works (Loidl et al. 2019; Loidl et al., 2020), so only a brief summary is given here. The initial source was prepared by electrodeposition of  $^{151}\text{Sm}$  on a silver foil, which was then repeatedly folded, laminated and annealed to break the samarium oxide/hydroxide layer formed during the electrodeposition process into small particles and incorporate them in the silver volume. The resulting silver foil had a thickness of approx. 7  $\mu\text{m}$  and was placed between two other silver foils, each 15  $\mu\text{m}$  thick, to ensure absorption of the full beta electron energy. These foils were then bonded together by diffusion welding and the final absorber, with a heat capacity of 18 pJ/K at 10 mK, was then fixed onto an MMC chip using Stycast 1266 epoxy resin. The MMC chip was chosen in line with the heat capacity of the absorber from a set of different MMC designs developed during the EMPIR project MetroBeta for a wide range of absorber heat capacities. The MMC signal was read out by a dc SQUID (Supracon model VC1A) and a Magnicon XXF-1 SQUID electronics; a Stanford Research Systems model SR560 low noise amplifier was used to further amplify the signal and to set an anti-aliasing filter.

An external photon-emitting source with about 9.9 kBq of  $^{55}\text{Fe}$  and approx. 260 Bq of  $^{109}\text{Cd}$  was used for energy calibration. The source was prepared by means of drop deposition on a gold disc (thickness 100  $\mu\text{m}$ ) using solutions with high radionuclidic purity. The gold disc was

then inserted into a holder made of gold-plated copper with a 4 mm diameter front hole. The radioactive source itself was covered with a 125  $\mu\text{m}$  thick beryllium disk to stop Auger and conversion electrons. A gold collimator placed between the calibration source and the silver absorber was used to obtain an appropriate count rate in the photon lines (about  $0.5 \text{ s}^{-1}$  in the 5.9 keV Mn  $K_{\alpha}$  line). The MMC was enclosed together with the SQUID and the collimated calibration source in a superconducting lead cylinder for magnetic shielding and mounted in a dilution refrigerator having a base temperature of about 10 mK.

### **3. Analysis of the data to obtain the emission spectrum**

The data were continuously recorded for 15 days at an operating temperature of about 10.3 mK. The detector temperature was not controlled and fluctuated by  $\sim (+ 0.3 \text{ mK}; - 0.15 \text{ mK})$ . Data analysis, including triggering, was performed completely offline to obtain the energy spectrum. This analysis was carried out with a custom-built code that was developed at LNHB using the MATLAB<sup>®</sup> environment. The pulse heights were estimated by optimal filtering. The final spectrum contained  $8.6 \cdot 10^6$  counts, about 5% of which were due to the calibration source of  $^{55}\text{Fe}$  and  $^{109}\text{Cd}$ . The pulse height drift over time caused by temperature fluctuations of the cryostat was corrected using the drift of the 5.9 keV X-ray line. Pile-up rejection was performed by a combination of an extendable dead time algorithm and a  $\chi^2$  criterion calculated by fitting a template pulse to the triggered pulses.

A second independent analysis was carried out using a Python<sup>™</sup>-based code newly developed at PTB. The analysis procedure was basically the same as that previously done at LNHB, but with a completely new implementation in a different programming language. The data was triggered for decay events, i.e., heat pulses in the detector, using a constant fraction discriminator trigger with an extendable dead time. Based on the identified events, an initial average pulse shape was calculated using manually chosen training pulses. This initial average

served as the seed for an iterative process to find a better-defined average pulse, which allowed the proper determination of the detected pulse heights (via optimal filtering) as well as other pulse properties. A  $\chi^2$  cut for pile-up rejection and a pulse height drift correction using events from the  $K_\alpha$  line emitted from the  $^{55}\text{Fe}$  source were also applied here. The final spectrum contained  $10.3 \cdot 10^6$  events.

The entire spectrum derived from the MMC measurement with the LNHB analysis is shown in Figure 2. The spectrum contains very pronounced peaks resulting from the external photon emitting source of  $^{55}\text{Fe}$  and  $^{109}\text{Cd}$ . The inner part of Figure 2 shows a magnification of the energy range from 21 keV to 26 keV to make clear that the Ag  $K_{\alpha 1}$  and Ag  $K_{\alpha 2}$  X-ray peaks, which occur as a consequence of the  $^{109}\text{Cd}$  decay, can be distinguished. In principle, these peaks could be analyzed in more detail to obtain more information on the X-ray emission (e.g., the ratio of probabilities). This objective, however, is being pursued by another experiment that is currently under way to measure X-ray emissions with even higher precision, and which is similar to the ultra-high energy resolution study of  $^{210}\text{Pb}$  photon emissions described by Rodrigues et al. (2021). In these experiments, any (disturbing) contribution caused by the embedded beta emitter is avoided.

Figure 2 also demonstrates the high energy resolution of the measurement, which was found to be about 45 eV (FWHM) at 6 keV and about 70 eV (FWHM) at 22 keV.

A closer look at the spectrum reveals further peaks (Figure 3), and it was possible to identify all pronounced peaks. It should be noted that most of the components of the setup immediately surrounding the detector are made of gold plated copper, while the collimator was made of gold and the absorber material was silver. Corresponding fluorescence peaks or escape peaks where these materials are involved were therefore expected.

In Figure 4, the spectrum from Figure 3 is compared with the spectrum obtained with the PTB analysis code. The latter spectrum contains more events and was scaled for better

comparability. A systematic and detailed comparison between the two analysis codes will be presented in a forthcoming article.

#### 4. Determination of the maximum beta energy

The maximum beta energy of  $^{151}\text{Sm}$  was determined by means of an analysis using Kurie plots as described in the following. The concept for Kurie plots (Kurie et al., 1936) is based on the assumption that the beta spectrum is described by

$$N(W)dW = \frac{G_{\beta}^2}{2\pi^3} F(Z,W) pW \cdot (W_0 - W)^2 dW \cdot X(W) \cdot C(W) r(Z,W) , \quad (1)$$

where  $N(W)$  corresponds to the measured data,  $F(Z,W)$  is the Fermi function,  $p = (W^2-1)^{1/2}$ ,  $W_0 = 1+E_{\text{max}}/m$ ,  $W = 1+E/m$  and  $G_{\beta}^2$  is a constant (squared product of the weak interaction coupling constant  $g$  and the cosine of the Cabibbo angle,  $\cos \theta_C$ ). In the traditional approach for Kurie plots, the functions  $C(W)$ ,  $X(W)$  and  $r(Z,W)$  are not used (i.e., set to unity). In this case, Equation (1) can be rearranged to get

$$\sqrt{\frac{N(W)}{F(Z,W)pW}} = K(W_0 - W) , \quad (2)$$

so that we obtain a linear function with  $K$  being the slope. The left-hand side of Equation (2) does not depend on the maximum energy  $W_0$ . Hence the Kurie plot (i.e., a linear fit of the data) can be used to determine  $W_0$ .

Here, however, we introduce  $X(W)$  as an additional correction that allows for screening and atomic exchange effects.  $C(W)$  denotes the shape factor function, which is  $C(W)=1$  for an allowed transition. The function  $r(Z,W)$  is a correction to account for the atomic overlap effect and is given by (Hayen et al., 2018)

$$r(Z, W) = 1 - \frac{1}{W_0 - W} \frac{\partial^2}{\partial Z^2} B(G) \quad (3)$$

with  $B'' = \frac{\partial^2}{\partial Z^2} B(G)$  being a constant. This quantity can be obtained from adjustments: For

$^{151}\text{Sm}$   $B'' = 0.262(13)$  keV. We used the parametrization stated by Hayen et al. (2018) to determine  $B''$  and estimate its relative uncertainty to be 5% uncertainty (Hardy and Towner, 2009).

In this case, Equation (1) can be rearranged to obtain

$$\sqrt{\frac{N(W)}{pWF(Z, W)X(W) \cdot C(W)}} = K \sqrt{(W_0 - W)^2 - B''(W_0 - W)} \quad (4).$$

The right side of the equation does no longer correspond to a linear function as in Equation (2), but it still represents a function with only two unknown parameters  $W_0$  and  $K$  which can be obtained from a fit procedure.

Although there are two beta branches, the analysis described in this section was carried out assuming just one beta transition. This is possible since, as mentioned earlier, the spectrum resulting from the transition to the excited state of  $^{151}\text{Eu}$  is shifted by the energy of the gamma transition in this measurement such that the endpoints of both beta spectra occur at the same energy. The presence of the weak second decay branch (of the same nature, i.e., first forbidden, non-unique) only slightly changes the slope of the linear fit function but does not change the intersection with the energy axis.

In the 80 keV to 85 keV range, the experimental spectrum contains neither beta events nor events from the external photon calibration sources. That is why this range was used to evaluate a background, which amounts to 0.2869 counts per bin when using a bin width of 20 eV. In order to study background effects, the background was assumed to be constant over the entire

spectrum and it was subtracted. In some bins at high energies, the background subtraction can result in negative bin contents. In such cases, we set  $N(W) = 0$  in order to avoid a negative radicand in Equation (4). However, this measure had no consequences for the Kurie fits since bins at high energies were not used. The analysis was also repeated without background subtraction and the difference was used as one component of uncertainty.

Figure 5 (left) shows a Kurie plot produced using a shape factor function  $C(W) = 1$  and with no correction applied for screening and the exchange effect. In particular, the high-energy part of the plot (Figure 5, right) shows that the data are well described with the Kurie fit. This confirms the findings from Achor et al. (1959) and Bé et al. (2015), who also found that the spectrum is well described with an allowed shape factor at high energies. The following analysis is thus based on the assumption that the shape factor is  $C(W) = 1$ , and experimental data at low energies ( $< 30$  keV) are ignored.

The details of the theoretical study of the two branches in  $^{151}\text{Sm}$  decay are given in Section 5. Figure 6 shows a corresponding Kurie plot when allowing for screening and the atomic exchange effect (both introduced via the energy dependent correction  $X(W)$ ). The corresponding Kurie plot yields a  $\chi^2$  that is just slightly lower than that shown in Figure 5. However, the fit procedure was repeated with different spectrum energy ranges applied (see Table 1), and these results show slightly less dependence on the selected energy range when screening and the atomic exchange effect are allowed for.

The overlap correction was found to be of very high importance. Ignoring this effect would lead to a maximum energy that is lower by about 132 eV. This is quite remarkable since it seems that the effect was not taken into account in the majority of historical analyses using Kurie plots.

The results of the fit procedure with various conditions applied are summarized in Table 1. The measurement results at high energies were not used when making Kurie fits in order to avoid any complications relating to a potential distortion of the recorded spectrum due to the finite energy resolution, a topic discussed in detail by Willett and Spejewski (1967) (see also Wortman and Cramer, 1964). This effect leads to an overestimation of counts at high energies, whereas the impact at medium energies is negligible. For this reason, we only used data of the spectrum below 74 keV when making Kurie plots. However, Table 1 contains some results that were obtained with higher accepted upper limits of the used energy range. But even these results are in reasonable agreement, possibly due to the excellent energy resolution in our experiment. In order to evaluate an uncertainty assigned to the energy resolution, a spectrum computed with the BetaShape program (see next section) was used as the input spectrum for the Kurie analysis and the known maximum beta energy was again determined. Then the spectrum was convoluted with a Gaussian function assuming a constant  $\sigma = 100$  eV (corresponds to approx. 236 eV FWHM). When using an energy range from 50 keV to 74 keV, a Kurie analysis with the modified spectrum yielded a maximum energy 1.2 eV greater than the one obtained with the initial spectrum. In a second step, the initially calculated spectrum was convoluted again, but this time allowing for an energy-dependent energy resolution. To this end, it was assumed that there is a linear relationship between the energy resolution and the energy. The linear function was obtained from the energy resolution determined at 6 keV (45 eV FWHM) and at 22 keV (70 eV FWHM). The Kurie fit of this spectrum gives a maximum beta energy 1.3 eV higher than the one derived from the initial spectrum when the energy range of 50 keV to 74 keV is used in both cases.

The uncertainty of the counts in a bin  $N(W)$  was assumed to be  $N^{1/2}$  and propagated to make weighted fit procedures possible. Some fits were also carried out with the weights ignored in order to evaluate one part of an uncertainty assigned to the fit procedure.

The maximum beta energy was found to be a bit lower when a wider range, extending down to 30 keV, is accepted. In this work, only those results obtained with ranges at high energies were used to produce the final result. The result without background subtraction and the result with an unweighted fit were only used for the uncertainty consideration (Table 2).

The results No. 1-16 in Table 1 were obtained using the spectrum as analyzed with the LNHB code, while results 17 and 18 come from a spectrum obtained with the new PTB code. When using the PTB code, the background, i.e., the mean content per 20 eV bin, is found to be about 0.4304 counts, nearly 1.5 times larger than the background determined by means of the LNHB code. One explanation might be that the codes apply different signal processing techniques that produce significant differences in the number of rejected events (relative deviation about 20%). The algorithms may also cause differences relating to the identification of pile-up events. This may also explain why the maximum beta energy is found to be slightly higher when the analysis is applied to the spectrum obtained with the PTB code. The corresponding difference is taken into account as one uncertainty component assigned to the analysis software and pile-up effect.

The uncertainty assigned to the model was evaluated by considering the changes that are observed when the correction for screening and the atomic exchange effect is ignored. The influence of the overlap correction was evaluated by varying  $B^*$  within its uncertainty when repeating the Kurie fit analyses.

The final result is the unweighted mean of selected data from Table 1 and was found to be  $E_{\max}=76.430(68)$  keV. A detailed uncertainty budget is shown in Table 2.

## 5. Theoretical calculation of the beta spectra

The general expression of the beta spectrum is given in Equation (1) in relativistic units ( $\hbar = m_e = c = 1$ ). The two transitions of the  $^{151}\text{Sm}$  decay are of the first forbidden non-unique

type, and are in principle sensitive to the structure of the initial and final nuclear levels. The very low  $Q$ -value makes them excellent candidates for the  $\xi$  approximation (Mougeot, 2015), as  $2\xi = 14.2 \text{ MeV} \gg E_{max}$  in both transitions. In this context, it is common to approximate them as allowed, without any nuclear structure information, i.e.,  $C(W) = 1$  in Equation (1). The details of the formalism, and its improvements, employed in the BetaShape code<sup>1</sup> for such transitions have been described elsewhere (Mougeot, 2015; Mougeot, 2017; Aprile et al., 2020). This released version of the code does not consider the correction factors  $C(W)$ ,  $X(W)$  and  $r(Z,W)$  in Equation (1). The  $X(W)$  correction corresponds to the atomic exchange effect calculated as described by Mougeot and Bisch (2014) and as complemented by Aprile et al. (2020). This effect has recently been extended to forbidden unique transitions as briefly described by Haselschwardt et al. (2020). The  $r(Z,W)$  term is the atomic overlap correction, which accounts for shake-up and shake-off effects due to the mismatch of initial and final atomic orbitals, and we applied the methodology stated by Hayen et al. (2018) to evaluate it.

However, the direct comparison of the predicted spectra with the high-precision measurement from this work has highlighted a significant discrepancy at very low energy, i.e., below 4 keV. For this reason, we have calculated the shape factor  $C(W)$  in order to quantify the accuracy of the  $\xi$  approximation in the case of the  $^{151}\text{Sm}$  decay. In Behrens and Böhning's formalism (Behrens and Böhning, 1971; Behrens and Böhning, 1982), the shape factor results from the double multipole expansion of both the nuclear and the lepton currents:

$$C(W) = \sum_{K, k_e, k_\nu} \lambda_{k_e} \left[ M_K^2(k_e, k_\nu) + m_K^2(k_e, k_\nu) - \frac{2\mu_{k_e} \gamma_{k_e}}{k_e W} M_K(k_e, k_\nu) m_K(k_e, k_\nu) \right]. \quad (5)$$

In this expression,  $k_e$  and  $k_\nu$  are quantum numbers of the leptons and quantities with a  $k_e$  subscript depend on the relativistic electron wave functions.  $K$  is the main multipole order that

---

<sup>1</sup> Code available at: <http://www.lnhb.fr/rd-activities/spectrum-processing-software/>

comes from the nuclear current expansion. Following Behrens and Bühring's recommendation, we considered  $K = 0, 1$  and  $k_e, k_\nu = 1, 2$  for the main transition of the  $^{151}\text{Sm}$  decay; and  $K = 1, 2$  and  $k_e, k_\nu = 1, 2, 3$  for the secondary transition. The  $M_K$  and  $m_K$  quantities include both the nuclear and the lepton matrix elements for the one-body transition operator (Mougeot, 2019).

In occupation number representation, a nuclear state is described by a many-particle wave function, which is a linear combination of nucleon wave functions. The transition amplitude is given by evaluating a one-body spherical tensor operator  $T_\lambda$  between the initial and final nuclear states and can be expressed as (Suhonen, 2007):

$$\langle \xi_f \mathbf{J}_f \| T_\lambda \| \xi_i \mathbf{J}_i \rangle = \hat{\lambda}^{-1} \sum_{a,b} \langle a \| T_\lambda \| b \rangle \langle \xi_f \mathbf{J}_f \| [c_a^\dagger \tilde{c}_b]_\lambda \| \xi_i \mathbf{J}_i \rangle,$$

where  $\hat{\lambda}$  is the tensor rank,  $\langle a \| T_\lambda \| b \rangle$  is a single-particle matrix element describing a nucleon-nucleon transition, and  $\langle \xi_f \mathbf{J}_f \| [c_a^\dagger \tilde{c}_b]_\lambda \| \xi_i \mathbf{J}_i \rangle$  is the one-body transition density that weights the contribution of the nucleon-nucleon transition. The list of nucleon-nucleon transitions and their weights must be given by a nuclear structure model.

It should be noted that the beta decay modeling has to be relativistic because of the small rest mass of the beta particle compared to the kinetic energies involved. The lepton and nucleon wave functions thus exhibit large and small components. This results in non-relativistic matrix elements that combine only the large components and in relativistic matrix elements that involve small components (Mougeot, 2019). Forbidden non-unique transitions are usually dominated by a relativistic vector matrix element (Behrens and Bühring, 1971). However, nuclear structure models are very often non-relativistic. The small (relativistic) component of a nucleon wave function can be estimated from its large (non-relativistic) component, but it has for decades been seen that this approximation is not accurate – see, e.g., Sadler and Behrens (1993) with respect to  $^{36}\text{Cl}$  decay. The usual approach is to consider the conserved vector

current (CVC) hypothesis, which comes from gauge invariance of the weak interaction and provides a relationship between non-relativistic and relativistic vector matrix elements (Behrens and Bühring, 1982). A key ingredient in this relationship is the Coulomb displacement energy  $\Delta E_c$ , for which an estimate is given below.

A realistic nuclear structure has been determined by means of the shell model code NuShellX@MSU (Brown and Rae, 2014). This code describes the nuclear levels considering an inert core and a valence space in which the nucleons above the core are distributed. Different interaction Hamiltonians are available for different mass regions, fitted in order to reproduce some experimental data. In the case of  $^{151}\text{Sm}$  and  $^{151}\text{Eu}$ , we selected the *jj56pn* valence space and used the recommended *khhe* effective interaction. Above the doubly-magic  $^{132}\text{Sn}$  core, 12 (13) protons ( $\pi$ ) can be distributed in the valence space spanning  $1g_{7/2}$  to  $1h_{11/2}$  and 7 (6) neutrons ( $\nu$ ) can be distributed in the valence space spanning  $1h_{9/2}$  to  $1i_{13/2}$  for  $^{151}\text{Sm}$  and  $^{151}\text{Eu}$ , respectively. The number of possible configurations is so high that the valence space must be constrained in order to limit the computational burden. This was done by filling the lowest orbitals and blocking the highest as: full  $\pi 1g_{7/2}$ ; minimum 2 in  $\pi 2d_{5/2}$ ; minimum 4 in  $\nu 1h_{9/2}$ ; empty  $\nu 3p_{1/2}$  and  $\nu 1i_{13/2}$ . The energy of the first excited states in  $^{151}\text{Eu}$  was found to be 98.1 keV, compared to the experimental value of 21.541 keV. As the beta transition from this state is small, this nuclear description is considered sufficiently accurate. The one-body transition densities for the dominant  $K$  values are given in Table 3 for the main beta transition and in Table 4 for the secondary transition.

The harmonic oscillator frequencies needed for the calculation of the single-particle matrix elements were determined following the method described by Towner et al. (1977). We used the experimental root mean square charge radii from Angeli and Marinova (2013) and the nucleon configurations provided by NuShellX. We obtained  $(\hbar\omega)_\nu = 8.197$  MeV for the initial neutrons and  $(\hbar\omega)_\pi = 7.348$  MeV for the final protons. We also deduced the equivalent

uniform charge radii and used them in the calculations:  $R_c(\text{Sm}) = 6.452 \text{ fm}$  and  $R_c(\text{Eu}) = 6.448 \text{ fm}$ . The Coulomb displacement energy, needed for applying the CVC hypothesis, can be expressed as:

$$\Delta E_c = \frac{3}{5} \frac{\alpha}{R_{cf}} Z_f (Z_f - 1) - \frac{3}{5} \frac{\alpha}{R_{ci}} Z_i (Z_i - 1)$$

where the  $i$  and  $f$  subscripts stand for *initial* and *final* nuclei, and  $\alpha$  denotes the fine structure constant. In the present case,  $\Delta E_c = 16.91 \text{ MeV}$ .

We observed a breakdown of the formalism of Behrens and Bühring (1982) when calculating the shape factors, a possibility pointed out by these authors in the case of very low energy transitions. To expand the lepton current, they expanded the electron wave functions in powers of  $(m_e R)$ ,  $(WR)$  and  $(\alpha Z)$ . This procedure is tractable thanks to the simplicity of the Coulomb potential for a uniformly charged sphere. At very low energy, quantities derived from the electron wave functions exhibit a divergence that can be avoided by introducing a screened potential, which gives a more realistic Coulomb potential. As the lepton current cannot be expanded any further, we reanalyzed the Behrens and Bühring formalism in order to calculate the  $M_K$  and  $m_K$  quantities with a lepton current determined numerically from the complete electron wave functions. For this reason, only the multipole expansion of the nuclear current is kept.

The theoretical shape factors without and with CVC hypothesis are given in Figures 7 and 8 for the main and secondary beta transitions in  $^{151}\text{Sm}$  decay, respectively, together with the atomic exchange corrections. Clearly, the atomic correction is much greater than the nuclear correction in both transitions. The shape factors exhibit a linear slope opposite to what would be needed to account for the discrepancy between theory and experiment below 4 keV. Inspecting the numerical values, we found that without the CVC hypothesis the  $M_1(1,1)$

quantity predominates, the next largest quantities being  $M_0(1,1)$ , lower by 3 orders of magnitude, and  $m_1(1,1)$ , lower by a factor of 20 to 100 according to the transition. With the CVC hypothesis,  $M_1(1,1)$  is relatively less predominant, with  $M_0(1,1)$  being only 20 times lower in the main transition, and  $m_1(1,1)$  just 10 times lower in the secondary transition. These quantities are the dominant quantities in allowed transitions (Behrens and Bühring, 1982), confirming the validity of the  $\xi$  approximation for  $^{151}\text{Sm}$ . However, one can see from Figures 7 and 8 that in the most realistic calculation (with CVC hypothesis), the  $\xi$  approximation is only accurate at the 5% precision level.

Finally, we estimated different uncertainty components for these calculations. It is clear that the central value, i.e., the reference spectrum, will be the most realistic, given that it takes account of the atomic exchange effect, the nuclear structure and the CVC hypothesis. The most direct uncertainty component that influences the spectrum shape and that must be taken into consideration comes from the uncertainty on  $E_{max}$ . Its impact is determined by calculating the spectrum at the two limit values  $E_{max} \pm u(E_{max})$ . The uncertainty propagation related to the  $r(Z,W)$  correction is also straightforward as explained in Section 4.

One important point to highlight concerns the procedure for the normalization of the calculated spectrum to the measured spectrum. Any constant factor independent of the particle energy cannot have an influence on the spectrum shape because its effect is absorbed by the normalization. This is why it is difficult to assess the uncertainty due to the atomic exchange effect. Taking, for example, a 5% shift on this correction does not change the spectrum shape at all. The only possibility would be to perform other calculations with a better atomic modeling and a correct determination of this effect for a forbidden non-unique transition, but this is beyond the scope of the present study. In the energy ranges employed for the fitting procedure

in the next section, however, we do not expect any significant change of the spectrum shape. We have thus not considered any uncertainty component for the atomic exchange effect.

The value of the axial-vector coupling constant  $g_A$  can have a strong influence on the spectrum shape (Kostensalo and Suhonen, 2017). For our calculations, we used  $g_A = 1.2763$  as the result of a simple mean of two recent precise measurements (Liu et al., 2010; Mund et al., 2013), which corresponds to the value for the free neutron decay. Because of the assumptions of the nuclear structure models to deal with the many-body problem, an effective  $g_A$  determined by comparison with some experimental observables may be necessary. Following Suhonen (2017), we determined an effective  $g_A$  of 1.1109 from the relationship given between infinite nuclear matter and finite nuclei. This value was chosen as a lower value of  $g_A$  and a symmetric upper value of 1.4417 was applied. Calculations with these two limits provide a conservative estimate of the uncertainty from the nuclear structure modeling.

The CVC hypothesis directly depends on the value of the Coulomb displacement energy  $\Delta E_C$ . A constant value is only an approximation, and it has been demonstrated (Damgaard and Winther, 1966) that this quantity can be very sensitive to the overlap of the initial and final nucleon wave functions. We have calculated  $\Delta E_C$  for the main nucleon-nucleon transitions of both branches, finding a systematic decrease of 10% to 25%. We have thus chosen a relative uncertainty of  $\pm 25\%$  on  $\Delta E_C$ . Calculations with these two limits provide a conservative estimate of the uncertainty from the beta decay modeling.

The fitting procedure used to determine the branching ratios requires a practical result like ‘minimum’ and ‘maximum’ spectra. For this purpose, we analyzed the effects of the different uncertainty components on the spectrum shape and combined them such as to maximize their total effect. These two combinations were used to calculate the ‘minimum’ and ‘maximum’ spectra.

## 6. Determination of the decay probabilities of the two beta branches

The measured MMC spectrum was also used to determine the probabilities of the two beta branches. Figure 9 again shows the measured spectrum, but here after subtraction of a background as determined from the content in the 80 keV to 85 keV range. The measured spectrum is shown with a bin width of 20 eV. The spectra of the two beta transitions were calculated with the same binning using the BetaShape code (see previous section) allowing for screening effects and the atomic exchange effect. For the beta transition to the ground state, the maximum beta energy  $E_{\max}=76.430$  keV, as determined in this work, was used. For the other transition, the maximum energy was assumed to be  $76.430$  keV -  $21.541$  keV =  $54.889$  keV. However, in Figure 9 this spectrum was then shifted by  $21.541$  keV. Both computed beta spectra were normalized. In a first and simple fit procedure, the beta spectrum of the ground state transition was scaled to match the measured spectrum. To this end, the energy range between  $12.5$  keV and  $20$  keV (ROI 1 in Figure 9) was used. This energy range was selected because it satisfied the condition of only containing contributions of the beta transition to the ground state and no contributions from the other beta branch or the external photon source. In addition, this region corresponds to an energy range in which the theoretical model seems to be reliable (discrepancies are still found at very low energies). In a second fit procedure, the sum of both spectra was compared with the measured spectrum, but only the beta spectrum to the excited level was scaled. Here, the energy range from  $29$  keV to  $50$  keV (ROI 2) was used since it is also free of other peaks.

We assume that only two beta branches (Figure 1) exist, namely  $P_{\beta,\text{ground}}+P_{\beta,\text{excited}} = 1$ . Hence the corresponding probabilities can easily be obtained from the two scaling factors determined from the fits or from the integrals of the two scaled beta spectra.

We obtain  $P_{\beta,\text{ground}}=99.31(11)\%$  and  $P_{\beta,\text{excited}}=0.69(11)\%$ . A corresponding residual plot is shown in Figure 10. An uncertainty budget is given in Table 5. As in the case of the maximum beta energy, the analysis was carried out with spectra obtained from the two analysis codes,

giving slightly different results. The corresponding relative deviation was used as one uncertainty component assigned to the analysis software and pile-up.

For the evaluation of an uncertainty component assigned to the beta spectrum calculation, the analysis was repeated with the ‘minimum’ and ‘maximum’ spectra as described in Section 5. The corresponding uncertainty is also a dominant component (see Table 5). It must be noted that the low-energy range of the beta spectrum is not used for this particular analysis. However, the discrepancy between theory and experiment in the low-energy range indicates that some effects may not have been fully factored into the calculation of the spectra (see also the discussion in the next section).

The uncertainty component assigned to the fit was determined by slightly varying the energy ranges (the ROIs) that were considered. The statistical uncertainty was estimated as follows. If we define the ratio of the two scaling factors (or the ratio of the two integrals of the scaled computed beta spectra after the fit procedure) as  $x$ , the probabilities are given by  $P_{\beta,\text{ground}} = x(1+x)^{-1}$  and  $P_{\beta,\text{excited}} = (1+x)^{-1}$ . The relative uncertainty of the ratio  $x$  was assumed to

$$\text{be } \frac{u(x)}{x} = \sqrt{\left(\frac{u(N_1)}{N_1}\right)^2 + \left(\frac{u(N_2)}{N_2}\right)^2}, \text{ with } N_1 \text{ being the number of counts in ROI 1 and } N_2 \text{ being}$$

the number of counts due solely to the beta transition to the excited state in ROI 2. The relative uncertainty of  $x$  was then propagated.

Due to the dimensions of the silver absorber, it is not possible for more than 5% of the gamma rays and more than 1% of the X-rays to escape. This means that only in some cases would the corresponding photons not release their full energy within the detector. Such events could then lead to false entries below 21.54 keV in the measured spectrum. The total internal conversion coefficient for the gamma transition,  $\alpha_{\text{t}}=27.6$  (Kibédi et al., 2008), is rather high, which is why only 3.5% of the transitions lead to gamma-ray emissions. Assuming that 5% of the gamma rays may not deposit their full energy in the absorber results in an escape probability of 0.175%. In the case of internal conversion, part of the overall energy could be transferred to

X-rays, which might also escape. Assuming that 1% of X-rays may not deposit their full energy in the absorber results in an additional escape probability of 0.965%. The overall escape probability is thus 1.14%, indicating that in 1.14% of beta transitions to the excited state, the corresponding decay events might be registered below 21.5 keV rather than above this energy. Thus we take an additional uncertainty component into account which is given by  $2 \cdot 1.14\% \cdot P_{\beta,\text{excited}}$ . The factor 2 is used to allow for the fact that events with an escape effect are not counted in ROI 2 but could be counted in ROI 1. The factor can be considered a conservative safety margin.

Our final results for  $P_{\beta,\text{ground}}=99.31(11)\%$  and  $P_{\beta,\text{excited}}=0.69(11)\%$  are in agreement with the values from the Decay Data Evaluation Project (DDEP) as stated by Bé et al. (2016) if expanded uncertainties with a coverage factor  $k=2$  are considered. The DDEP values (99.07(4)% and 0.93(4)%) are based on a combination of an evaluated result for the gamma-ray emission intensity and the corresponding internal conversion coefficient (ICC). The evaluated gamma-ray emission intensity is dominated by one measurement carried out by Shen et al. (2011). That group combined gamma-ray spectrometry with liquid scintillation counting for activity measurements (see also He et al., 2009). The group also found small amounts of radioactive impurities in the used material. Hence, our results can be considered an independent and important supplement that does not require any assumption of the ICC. Unfortunately, the overall uncertainties of our results are slightly higher.

Of course, Figure 9 also makes it possible to compare theory and experiment. While a very good agreement can be observed over large parts of the spectrum, quite large deviations are discernible in the low-energy range below approx. 4 keV. These deviations were, in fact, a key motivation to analyze the MMC data with a second independent approach. This approach, however, confirmed the previous result. The remaining deviation will be discussed in the next section.

## 7. Discussion

The analysis presented in this paper demonstrates that MMC measurements can be used to determine maximum beta energies with very high precision. In addition, it was shown that even beta decay probabilities of two different branches could be determined, though in the presented case the corresponding uncertainties are higher than those obtained when using gamma-ray spectrometry in combination with an ICC.

The paper also makes clear that the experimental data and the theoretical calculations do agree over a wide energy range. However, significant discrepancies are still observed at very low energy, below 4 keV, even if this does not affect the determination of the  $Q$ -value. It should be noted that much better agreement was obtained for the allowed beta transition of  $^{63}\text{Ni}$  and the first forbidden non-unique beta transition of  $^{241}\text{Pu}$ . With a lower  $Q$ -value of 20.78(17) keV (Wang et al., 2021) and a higher  $Z$ ,  $^{241}\text{Pu}$  decay is a perfect case study of the  $\xi$  approximation and can be very confidently calculated as allowed. Hence, one can suspect that our theoretical description of non-unique beta transitions is still incomplete. We have demonstrated that the shape factor, and thus the nuclear structure model, cannot explain this discrepancy. However, we have approximated the atomic exchange correction by applying it as was done in the case of the forbidden unique transitions, i.e., on the  $\lambda_{k_e}$  parameters in the shape factor (Haselschwardt et al., 2020). A more reliable description should consider the exact convolution of the nuclear current with a lepton current that would include the atomic structure. Another possibility may be that our atomic wave functions are not sufficiently accurate for Sm and Eu. These two aspects are beyond the scope of the present work and will be addressed in the course of the EMPIR project PrimA-LTD.

On the other hand, it should also be noted that MMC sample preparation is difficult, and both the measurements and the subsequent analyses are very challenging – in particular in the low-energy range. However, the fact that the two more or less independent analysis codes yield

very similar spectrum shapes serves to increase confidence. We also considered a potential impact of electrons originating from the external calibration source. When using a simple PENELOPE Monte Carlo simulation (Salvat, 2015), it was confirmed that even conversion electrons from the  $^{109m}\text{Ag}$  isomer with the highest possible energy of 87.7 keV cannot pass the beryllium window.

The portion of events in the range from 0 keV to 4 keV which are due to the radioactive impurities  $^{154}\text{Eu}$  and  $^{155}\text{Eu}$  was estimated to be about  $6 \cdot 10^{-6}$ . There are two main explanations for this very low proportion. First, many decay events of both Europium isotopes are accompanied by low-energetic gamma-ray transitions, which have a high probability for internal conversion. Consequently, a shift in the beta spectra is to be expected similar to that seen in the case of the  $^{151}\text{Sm}$  beta decay to the excited level of  $^{151}\text{Eu}$ . For example, about 88.8% of the decay events of  $^{154}\text{Eu}$  coincide with the 123 keV gamma-ray transition, which will lead to internal conversion in about 54.5% of this transition. This means that about one half of all  $^{154}\text{Eu}$  decay events are shifted to an energy range beyond the  $^{151}\text{Sm}$  endpoint energy. The second reason for the low portion at low energies is the fact that  $^{154}\text{Eu}$  in particular has a high maximum beta energy ( $Q^- = 1968.4$  keV, Bé et al., 2004), so the overall spectrum is distributed over a much wider range than in the case of  $^{151}\text{Sm}$ .

As concerns the achievement of high-precision beta spectrum measurements at very low energies, a new experiment planned as part of the EMPIR project PrimA-LTD seems promising. Here, a source of  $^{129}\text{I}$  will be used, and it is anticipated that MMCs will produce accurate measurements even in the low-energy part of the beta spectrum of the dominant second forbidden non-unique transition. A special feature of this transition is that it is in coincidence with a low-energy gamma transition dominated by internal conversion. When considering a  $4\pi$  geometry, this transition causes a shift of the beta spectrum by the gamma-transition energy (about 39.6 keV), making it possible to measure the beta spectrum down to virtually 0 keV. In

addition, decay probabilities of both beta branches can then be determined, as was demonstrated in this work for  $^{151}\text{Sm}$ .

## Acknowledgments

This project, 20FUN04 PrimA-LTD, has received funding from the EMPIR program co-financed by the Participating States and from the European Union's Horizon 2020 research and innovation program. Moreover, we acknowledge support from several co-authors of our previous works (Loidl et al., 2019; Loidl et al., 2020) who contributed in various ways to make the  $^{151}\text{Sm}$  measurements possible.

## References

- Achor, W.T., Phillips, W.E., Hopkins, J.I., Haynes, S.K., 1959. Low-intensity conversion lines from  $\text{Sm}^{151}$  and  $\text{Sn}^{113}$ . *Phys. Rev.* 114, 137-142.
- Angeli, I., Marinova, K.P., 2013. Table of experimental nuclear ground state charge radii: An update. *At. Data and Nucl. Data Tables* 99, 69-95.
- Aprile, E. et al., 2020. Excess electronic recoil events in XENON1T. *Phys. Rev. D* 102, 072004.
- Bé M.-M., Chisté V., Dullieu C., Browne E., Chechev V., Kuzmenko N., Helmer, R., Nichols A., Schönfeld, E., Dersch R., 2004. Monographie BIPM-5: Table of radionuclides (Vol 2. – A=151 to 242), Bureau International des Poids et Mesures, Sèvres, ISBN 92-822-2207-1.
- Bé, M.M., Isnard, H., Cassette, Ph., Mougéot, X., Lourenço, V., Altitzoglou, T., Pommé, S., Rožkov, A., Auerbach, P., Sochorová, J., Dziel, T., Dersch, R., Kossert, K., Nähle, O., Krivošík, M., Ometáková, J., Stadelmann, G., Nonell, A., Chartier, F., 2015. Determination of the  $^{151}\text{Sm}$  half-life. *Radiochimica Acta* 103, 619-626.

- Bé, M.-M., Chisté, V., Dulieu, C., Kellett, M.A., Mougeot, X., Aric, A., Chechev, V.P., Kuzmenko N.K., Kibédi T., Luca, A., Nichols A.L., 2016. Monographie BIPM-5: Table of radionuclides (Vol. 8., A=41 to 198). Bureau International des Poids et Mesures, Sèvres, ISBN-13 978-92-822-2264-5.
- Behrens, H., Bühring, W., 1971. Nuclear beta decay. Nucl. Phys. A 162, 111-144.
- Behrens, H., Bühring, W., 1982. Electron Radial Wave Functions and Nuclear Beta Decay. Clarendon, Oxford.
- Broda, R., Cassette, P., Kossert, K., 2007. Radionuclide Metrology using liquid scintillation counting. Metrologia 44, S36-S52.
- Brown, B.A., Rae, W.D.M., 2014. The Shell-Model Code NuShellX@MSU. Nucl. Data Sheets 120, 115-118.
- Collé, R., 2007. Classical radionuclidic calorimetry. Metrologia 44, S118-S126.
- Damgaard, J., Winther, A., 1966. Use of conserved vector current theory in first forbidden  $\beta$ -decay. Physics Letters 23 (6), 345-346.
- Garcia-Toraño, E., Grau Malonda, A., 1985. EFFY, a new program to compute the counting efficiency of beta particles in liquid scintillators. Comput. Phys. Comm. 36, 307-312.
- Grau Malonda, A., 1999. Free parameter models in liquid scintillation counting. Colección Documentos CIEMAT. CIEMAT, ISBN 84-7834-350-4.
- Hardy, J.C., Towner, I.S., 2009. Superallowed  $0^+ \rightarrow 0^+$  nuclear  $\beta$  decays: A new survey with precision tests of the conserved vector current hypothesis and the standard model. Phys. Rev. C 79, 055502.
- Haselschwardt, S.J., Kostensalo, J., Mougeot, X., Suhonen, J., 2020. Improved calculations of  $\beta$  decay backgrounds to new physics in liquid xenon detectors. Phys. Rev. C 102, 065501.
- Hayen, L., Severijns, N., Bodek, K., Rozpedzik, D., Mougeot, X., 2018. High precision analytical description of the allowed  $\beta$  spectrum shape. Rev. Mod. Phys. 90, 015008.

- He, M, Shen, H., Shi, G., Yin, X., Tian, W., Jiang, S., 2009. Half-life of  $^{151}\text{Sm}$  remeasured. *Phys. Rev. C* 80, 064305.
- Kibédi, T., Burrows, T.W., Trzhaskovskaya, M.B., Davidson, P.M., Nestor, C.W. (Jr.), 2008. Evaluation of theoretical conversion coefficients using BrIcc. *Nucl. Instrum. Meth. A* 589, 202-229. And: <http://bricc.anu.edu.au/> (accessed June 2021).
- Kossert, K., Nähle, O., Grau Carles, A., 2011. Beta shape-factor function and activity determination of  $^{241}\text{Pu}$ . *Appl. Radiat. Isot.* 69, 1246-1250.
- Kossert, K., Grau Carles, A., Nähle, O., 2011. Čerenkov counting and liquid scintillation counting of  $^{36}\text{Cl}$ . LSC2010, *Advances in Liquid Scintillation Spectrometry: Proceedings of the 2010 International Conference on Liquid Scintillation Spectrometry, Paris, France, 6-10 September 2010*, edited by Philippe Cassette, in *Radiocarbon*, 2011, the University of Arizona, Tucson, Arizona, USA, ISBN 978-0-9638314-7-7, 161-170.
- Kossert, K., Grau Carles, A., Nähle, O.J., 2014. Improved Čerenkov counting techniques based on a free-parameter model. *Appl. Radiat. Isot.* 86, 7-12.
- Kossert, K., Mougeot, X., 2015. The importance of the beta spectrum calculation for accurate activity determination of  $^{63}\text{Ni}$  by means of liquid scintillation counting. *Appl. Radiat. Isot.* 101, 40-43.
- Kossert, K., Marganec-Gałązka, J., Mougeot, X., Nähle, O.J., 2018. Activity determination of  $^{60}\text{Co}$  and the importance of its beta spectrum. *Appl. Radiat. Isot.* 134, 212-218.
- Kostensalo, J., Suhonen, J., 2017.  $g_A$ -driven shapes of electron spectra of forbidden  $\beta$  decays in the nuclear shell model. *Phys. Rev. C* 96, 024317.
- Kurie, F.N.D., Richardson, J.R., Paxton, H.C., 1936. The radiations emitted from artificially produced radioactive substances. *Phys. Rev.* 49, 368-381.
- Liu, J. et al., 2010. Determination of the axial-vector weak coupling constant with ultracold neutrons. *Phys. Rev. Lett.* 105, 181803.

- Loidl, M., Rodrigues, M., Censier, B., Kowalski, S., Mougeot, X., Cassette, P., Branger, T., Lacour, D., 2010. First measurement of the beta spectrum of  $^{241}\text{Pu}$  with a cryogenic detector. *Appl. Radiat. Isot.* 68, 1454-1458.
- Loidl, M., Rodrigues, M., Le-Bret, C., Mougeot, X., 2014. Beta spectrometry with metallic magnetic calorimeters. *Appl. Radiat. Isot.* 87, 302-305.
- Loidl, M., Beyer, J., Bockhorn, L., Enss, C., Kempf, S., Kossert, K., Mariam, R., Nähle, O., Paulsen, M., Ranitzsch, P., Rodrigues, M., Schmidt, M., 2019. Beta Spectrometry with Metallic Magnetic Calorimeters in the Framework of the European EMPIR project MetroBeta. *Appl. Radiat. Isot.* 153, 108830.
- Loidl, M., Beyer, Bockhorn, L., J., Bonaparte, J.J., Enss, C., Kempf, S., Kossert, K., Mariam, R., Nähle, O., Paulsen, M., Ranitzsch, P.C.-O., Rodrigues, Wegner, M., 2020. Precision measurements of beta spectra using metallic magnetic calorimeters within the European Metrology Research Project MetroBeta. *J. Low Temp. Phys.* 199,451-460, <https://doi.org/10.1007/s10909-020-02398-2>.
- Mougeot, X., Bisch, C., 2014. Consistent calculation of the screening and exchange effects in allowed  $\beta^-$  transitions. *Phys. Rev. A* 90, 012501.
- Mougeot, X., 2015. Reliability of usual assumptions in the calculation of  $\beta$  and  $\nu$  spectra. *Phys. Rev. C* 91, 055504; Erratum *Phys. Rev. C* 92, 059902(E).
- Mougeot, X., 2017. BetaShape: a new code for improved analytical calculations of beta spectra. *EPJ Web Conf.* 146, 12015.
- Mougeot, X., 2019. Towards high-precision calculation of electron capture decays. *Appl. Radiat. Isot.* 154, 108884.
- Mund, D. et al., 2013. Determination of the weak axial vector coupling  $\lambda = g_A/g_V$  from a measurement of the  $\beta$ -asymmetry parameter  $A$  in neutron beta decay. *Phys. Rev. Lett.* 110, 172502.
- Rodrigues, M., Cassette, Ph., Lépy, M.C., Loidl, M., Ménesguen, Y., 2021. Determination of

- absolute photon emission intensities of  $^{210}\text{Pb}$ . *Appl. Radiat. Isot.* 109, 500-506.
- Rotzinger, H., Linck, M., Burck, A., Rodrigues, M., Loidl, M., Leblanc, E., Fleischmann, L., Fleischmann, A., Enss, C., 2008. Beta spectrometry with magnetic calorimeters. *J. Low Temp. Phys.* 151, 1087-1093.
- Sadler, R., Behrens, H., 1993. Second-forbidden beta-decay and the effect of (V+A)- and S- interaction admixtures:  $^{36}\text{Cl}$ . *Z. Phys. A* 346, 25-33.
- Salvat, F., 2015. Penelope-2014: A Code System for Monte Carlo Simulation of Electron and Photon Transport. OECD/NEA Data Bank, Issy-les-Moulineaux, France (NEA/NSC/DOC(2015) 3).
- Shen, H., He, M., Ruan, X.D., Dong, K., Jiang, S., 2011. Determination of the emission probability of the 21.54 keV  $\gamma$  ray in the decay of  $^{151}\text{Sm}$ . *Phys. Rev. C* 84, 054307.
- Suhonen, J., 2007. *From Nucleons to Nucleus: Concepts of Microscopic Nuclear Theory*. Springer, Berlin.
- Suhonen, J., 2017. Value of the Axial-Vector Coupling Strength in  $\beta$  and  $\beta\beta$  Decays: A Review. *Front. Phys.* 5:55, 1-35.
- Towner, I.S., Hardy, J.C., Harvey, M., 1977. Analogue symmetry breaking in superallowed Fermi  $\beta$ -decay. *Nucl. Phys. A* 284, 269-281.
- Wang, M., Huang, W.J., Kondev, F.G., Audi, G., 2021. The AME2020 atomic mass evaluation (II). Tables, graphs and references. *Chin. Phys. C* 45, 030003.
- Willett, J.B., Spejewski, E.H., 1967. A method for resolution correction and shape factor analysis of beta spectra. *Nucl. Instrum. Meth.* 52, 77-85.
- Wortman, D.E., Cramer, J.G., 1964. The correction of resolution distortion in continuous pulse-height spectra. *Nucl. Instrum. Method.* 26, 257-262.

**Table 1**

Results for the maximum beta energy  $E_{\max}$  obtained from a Kurie plot analysis with different conditions. Only No. 4-5, 10-13 and 15-18 were used to calculate the final result, which is  $(76.430 \pm 0.068)$  keV.

No.	Weighted fit?	Background subtracted?	Screening and exchange taken into account?	Energy range used for fit	$E_{\max}$ in keV	Used for final result?	Deviation from final result in eV
1	yes	yes	no	30 keV - 74 keV	76.290	no	-140
2	yes	yes	no	40 keV - 74 keV	76.360	no	-70
3	yes	yes	no	50 keV - 74 keV	76.384	no	-46
4	yes	yes	no	60 keV - 74 keV	76.425	yes	-5
5	yes	yes	no	60 keV - 72 keV	76.415	yes	-15
6	yes	yes	no	60 keV - 76 keV	76.429	no	-1
7	yes	no	no	60 keV - 74 keV	76.463	no	33
8	no	yes	no	60 keV - 74 keV	76.425	no	-5
9	yes	yes	yes	30 keV - 74 keV	76.360	no	-70
10	yes	yes	yes	40 keV - 74 keV	76.397	yes	-33
11	yes	yes	yes	50 keV - 74 keV	76.401	yes	-29
12	yes	yes	yes	60 keV - 74 keV	76.432	yes	2
13	yes	yes	yes	60 keV - 72 keV	76.425	yes	-5
14	yes	yes	yes	60 keV - 76 keV	76.434	no	4
15	yes	no	yes	60 keV - 74 keV	76.470	yes	40
16	no	yes	yes	60 keV - 74 keV	76.432	yes	2
17	yes	yes	yes	60 keV - 72 keV	76.460	yes	30
18	yes	yes	yes	60 keV - 74 keV	76.441	yes	11

**Table 2**

Uncertainty budget for the maximum beta energy  $E_{\max}$ . All uncertainties are stated as standard uncertainties ( $k = 1$ ).

Uncertainty component	$u$ in eV	Relative uncertainty	Comment
Energy calibration, binning	15	0.020%	Several well-known peaks used for the calibration, high reproducibility
Resolution distortion effect, finite energy resolution	20	0.026%	High-energy bins avoided, energy resolution (FWHM) is 45 eV at 6 keV and 70 eV at 25 keV, low energy dependence
Background	38	0.050%	Background taken into account
Fit method	36	0.047%	Variation of energy range; weighted vs. unweighted fit
Model	15	0.020%	Analysis with/without screening and atomic exchange effect; atomic overlap correction
Analysis software/pile-up	32	0.042%	Deviation when using input spectrum obtained from the two analysis codes
<b>Combined</b>	<b>68</b>	<b>0.089%</b>	

**Table 3**

One-body transition densities (OBTD) of the dominant multipole orders ( $K = 0, 1$ ) in the main transition of  $^{151}\text{Sm}$  decay.

$\nu \rightarrow \pi$	OBTD
$K = 0$	
$2f_{5/2} \rightarrow 2d_{5/2}$	-0.00725
$3p_{3/2} \rightarrow 2d_{3/2}$	0.01320
$K = 1$	
$2f_{7/2} \rightarrow 2d_{5/2}$	-0.00025
$2f_{5/2} \rightarrow 2d_{5/2}$	-0.02969
$3p_{3/2} \rightarrow 2d_{5/2}$	0.00062
$2f_{5/2} \rightarrow 2d_{3/2}$	-0.00213
$3p_{3/2} \rightarrow 2d_{3/2}$	0.00115
$3p_{3/2} \rightarrow 3s_{1/2}$	0.01442

**Table 4**

One-body transition densities (OBTD) of the dominant multipole orders ( $K = 1, 2$ ) in the secondary transition of  $^{151}\text{Sm}$  decay.

$\nu \rightarrow \pi$	OBTD
<b><math>K = 1</math></b>	
$2f_{7/2} \rightarrow 2d_{5/2}$	0.00461
$2f_{5/2} \rightarrow 2d_{5/2}$	-0.03577
$3p_{3/2} \rightarrow 2d_{5/2}$	-0.00957
$2f_{5/2} \rightarrow 2d_{3/2}$	0.00393
$3p_{3/2} \rightarrow 2d_{3/2}$	-0.00025
$3p_{3/2} \rightarrow 3s_{1/2}$	0.01557
<b><math>K = 2</math></b>	
$1h_{9/2} \rightarrow 2d_{5/2}$	0.14599
$2f_{7/2} \rightarrow 2d_{5/2}$	0.01031
$2f_{5/2} \rightarrow 2d_{5/2}$	-0.02588
$3p_{3/2} \rightarrow 2d_{5/2}$	-0.00050
$2f_{7/2} \rightarrow 2d_{3/2}$	0.00262
$2f_{5/2} \rightarrow 2d_{3/2}$	-0.00310
$3p_{3/2} \rightarrow 2d_{3/2}$	-0.00245
$2f_{5/2} \rightarrow 3s_{1/2}$	0.04081
$3p_{3/2} \rightarrow 3s_{1/2}$	-0.00353

**Table 5**

Uncertainty budget for the probability of the beta transition to the ground state of  $^{151}\text{Eu}$   $P_{\beta,\text{ground}}$ .

Uncertainty component	Relative uncertainty	Comment
Analysis software/pile-up	0.07%	Deviation when using input spectra obtained from the two analysis codes
Beta spectrum model	0.06%	Dependence on shape of computed spectra and propagated uncertainty for the atomic overlap correction
Fit	0.05%	Obtained from variation of fit ranges and weighted vs. unweighted fits
Statistics	0.01%	Propagated from Poisson uncertainties
Photon escape	0.02%	X-rays and gamma rays may not deposit their full energy
<b>Combined</b>	<b>0.11%</b>	

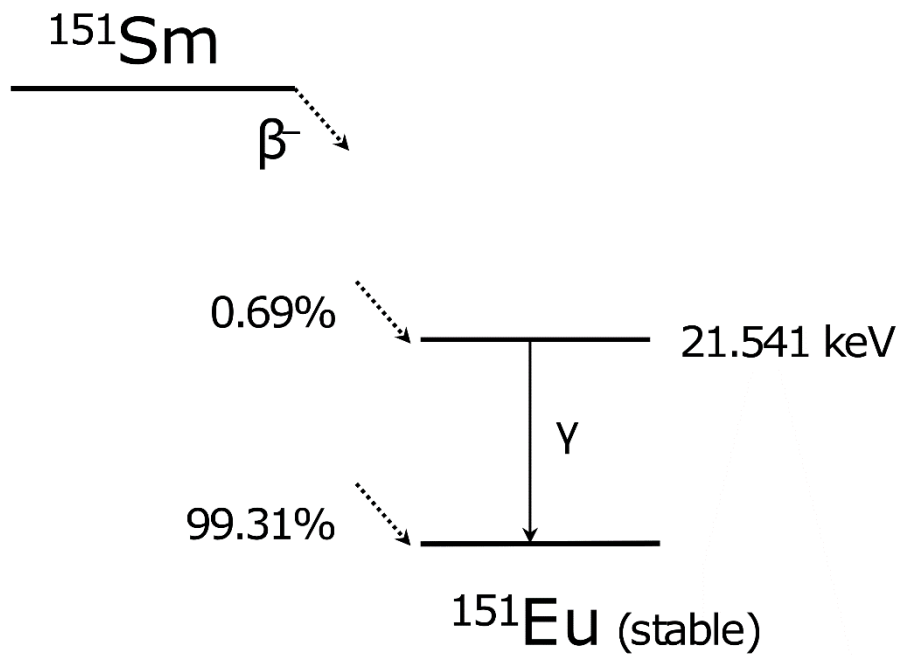


**Figure 1**

Decay scheme of  $^{151}\text{Sm}$ . The stated probabilities of the two beta branches correspond to the results from this work.

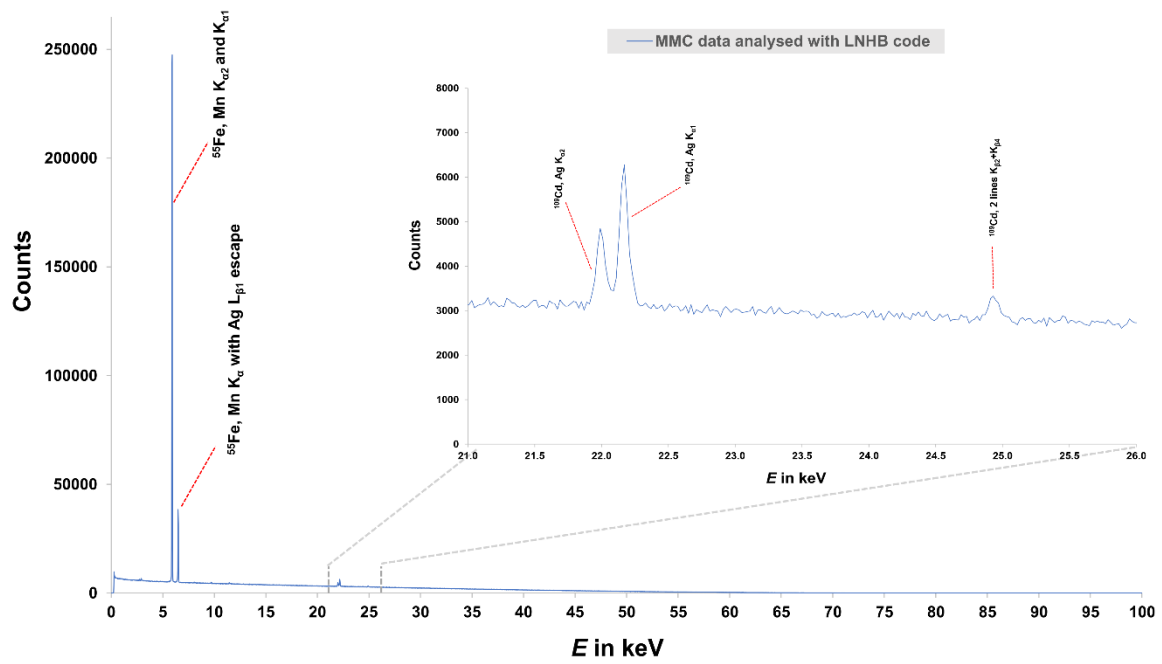


**Figure 2**

Measured MMC spectrum with an embedded  $^{151}\text{Sm}$  source and external  $^{55}\text{Fe}$  and  $^{109}\text{Cd}$  photon sources for the energy calibration. The inner diagram shows a magnification of the spectrum in the range from 21 keV to 26 keV.

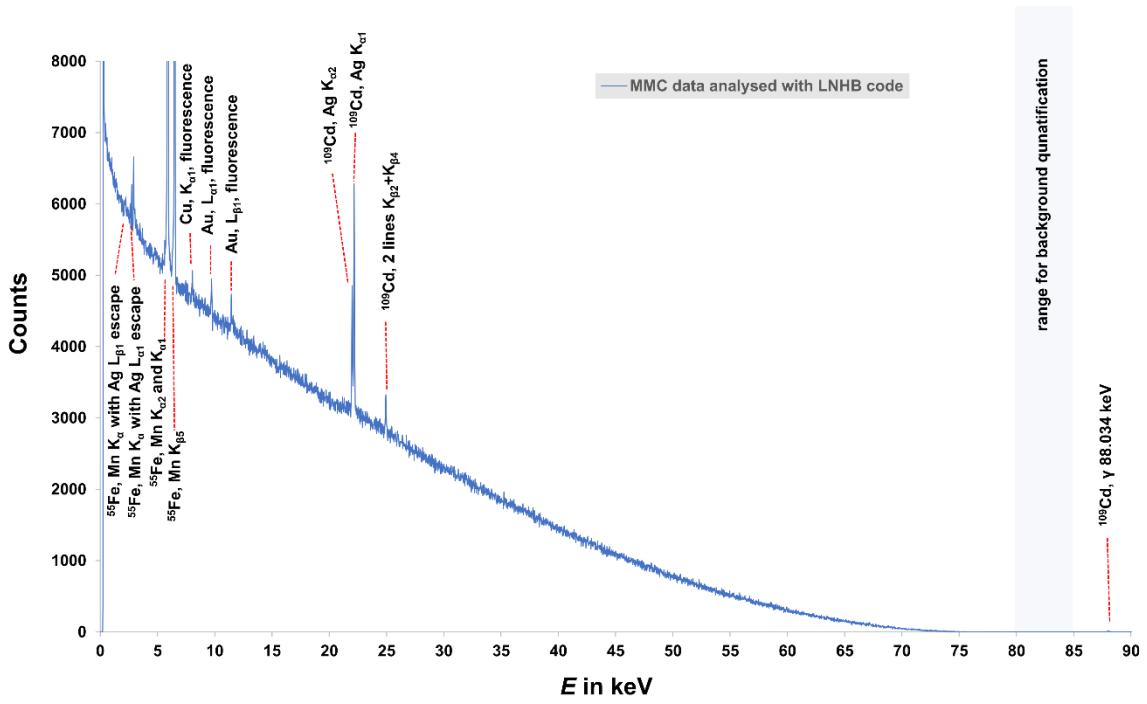


**Figure 3**

Measured MMC spectrum as shown in Figure 1, but with lower range at the ordinate. Relevant peaks in the spectrum are of known origin.

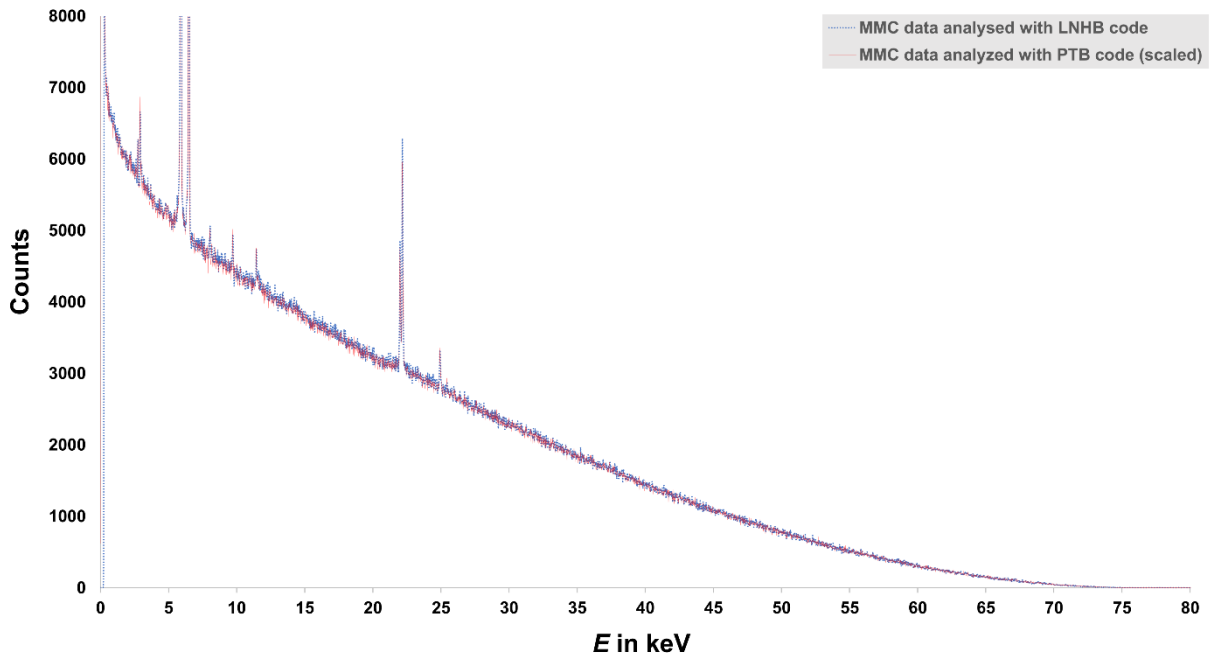


**Figure 4**

The raw data from the MMC measurement were analyzed with two different codes that yielded very similar spectra. The spectrum obtained with the PTB code contains more events and was therefore scaled with a factor of 0.882.

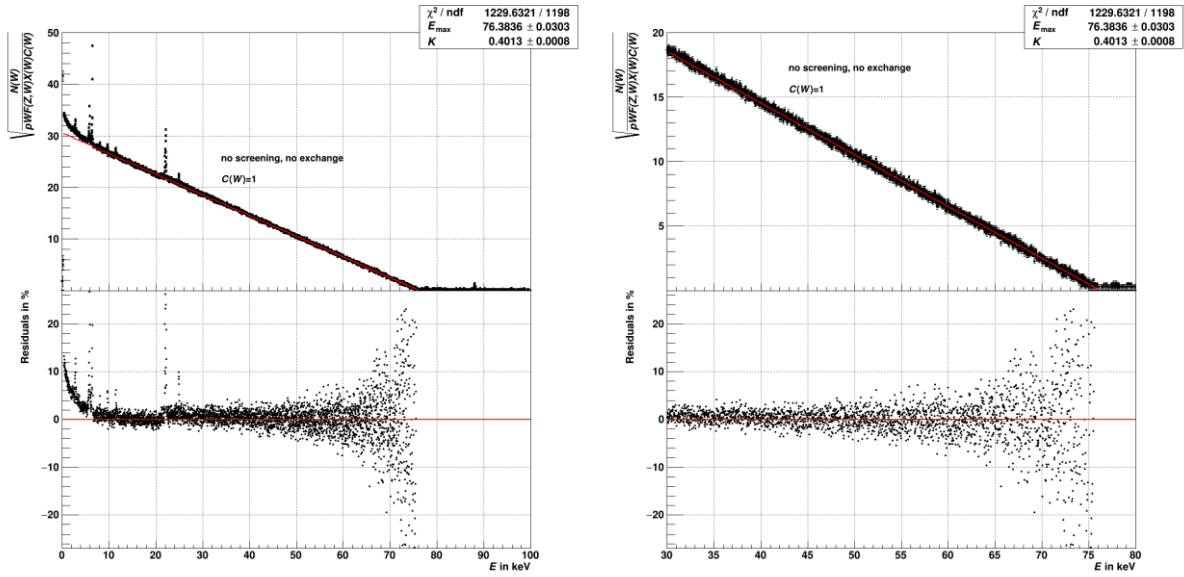


**Figure 5**

Kurie plot assuming a shape-factor function  $C(W)=1$ . No correction was applied for screening and the atomic exchange effects ( $X(W)=1$ ). For the fit procedure, the experimental data in the range from 50 keV to 74 keV were taken into account. The fit function (Eq. 4) also accounts for the overlap correction. The figure on the right shows the high energy part of the complete Kurie plot shown on the left. Residuals (bottom) are only shown in the energy range below the maximum beta energy.

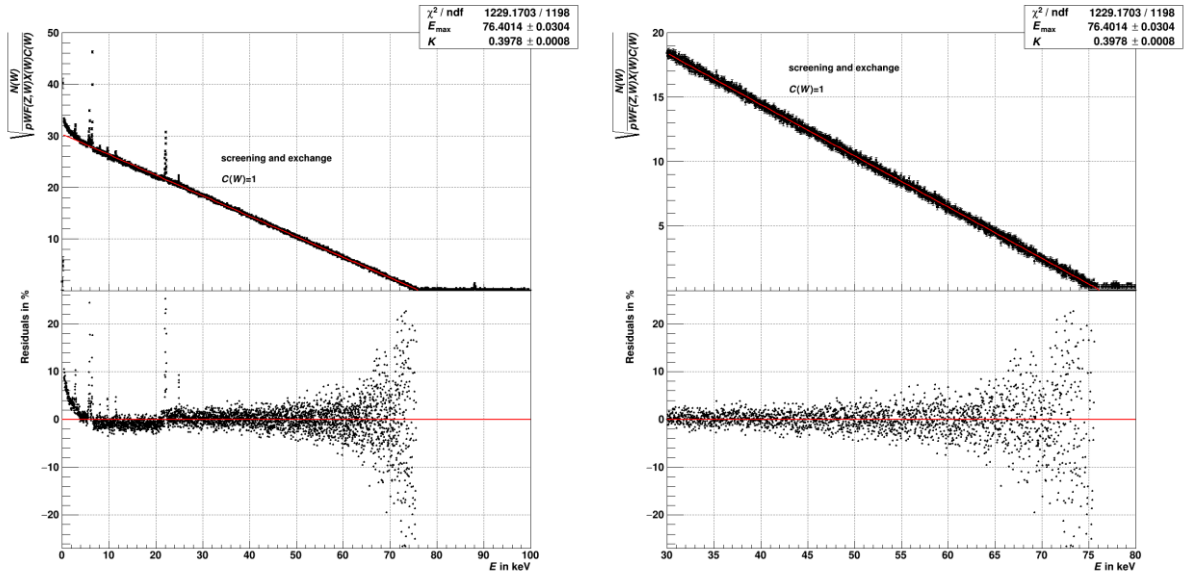


**Figure 6**

Kurie plot assuming a shape-factor function  $C(W)=1$  and taking screening and the atomic exchange effects into account. The fit function (Eq. 4) also accounts for the overlap correction. For the fit procedure, the experimental data in the range from 50 keV to 74 keV were used. The figure on the right shows the high energy part of the complete Kurie plot shown on the left. Residuals (bottom) are only shown in the energy range below the maximum beta energy.

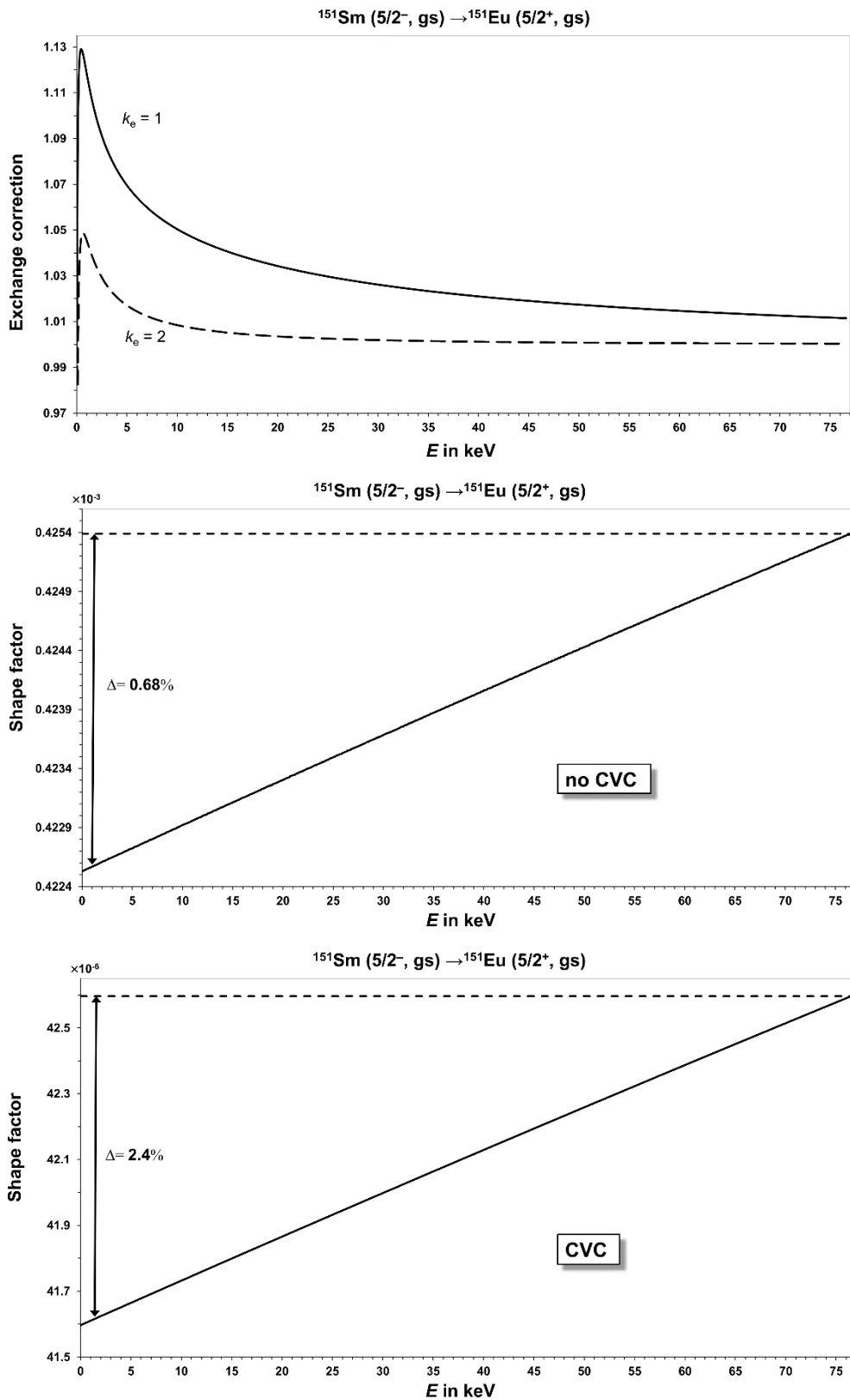


**Figure 7**

Atomic exchange corrections (*top*) and shape factors determined without (*middle*) and with (*bottom*) conserved vector current (CVC) hypothesis for the main first forbidden non-unique beta transition in  $^{151}\text{Sm}$  decay.

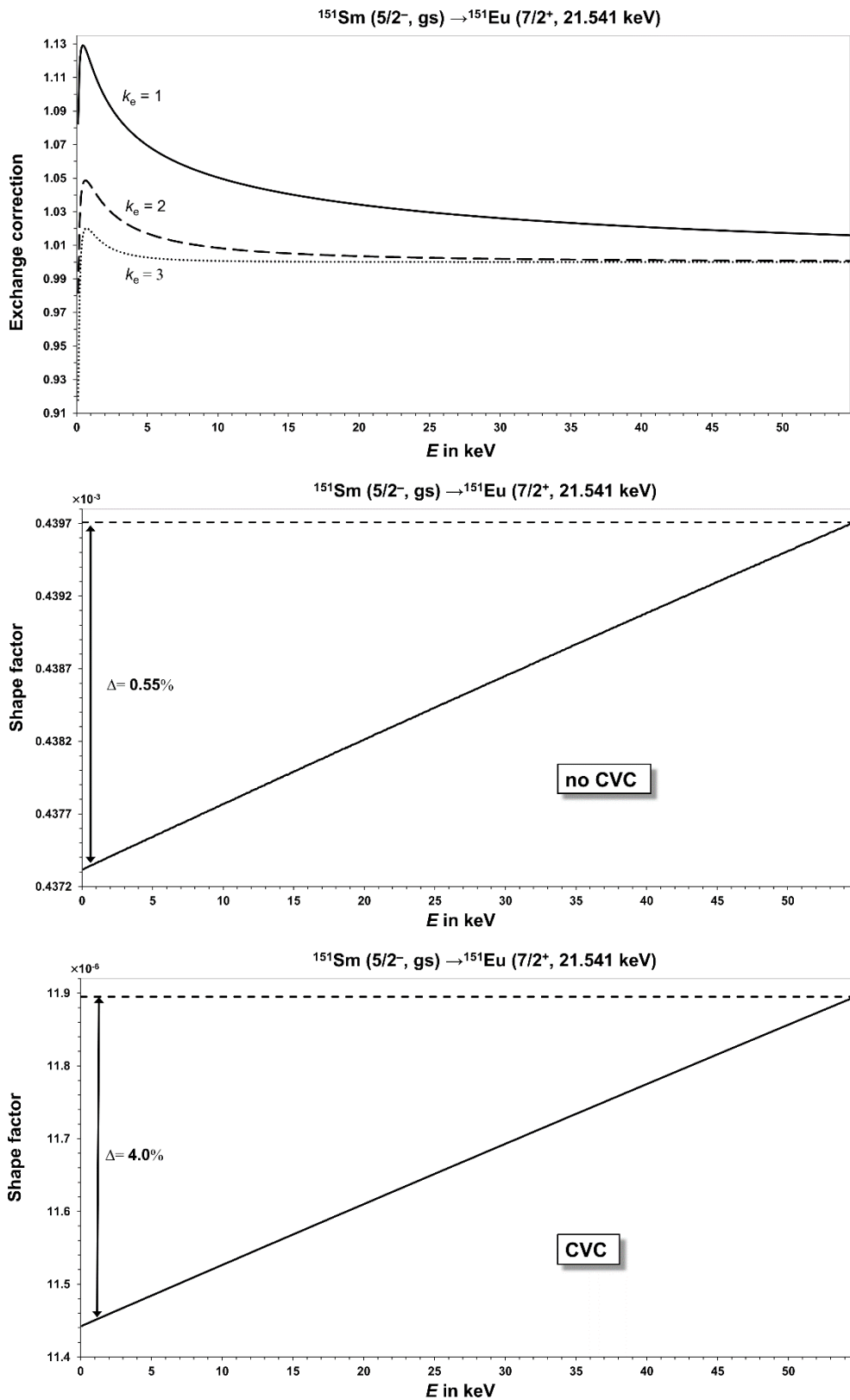


**Figure 8**

Atomic exchange corrections (*top*) and shape factors determined without (*middle*) and with (*bottom*) conserved vector current (CVC) hypothesis for the secondary first forbidden non-unique beta transition in  $^{151}\text{Sm}$  decay.

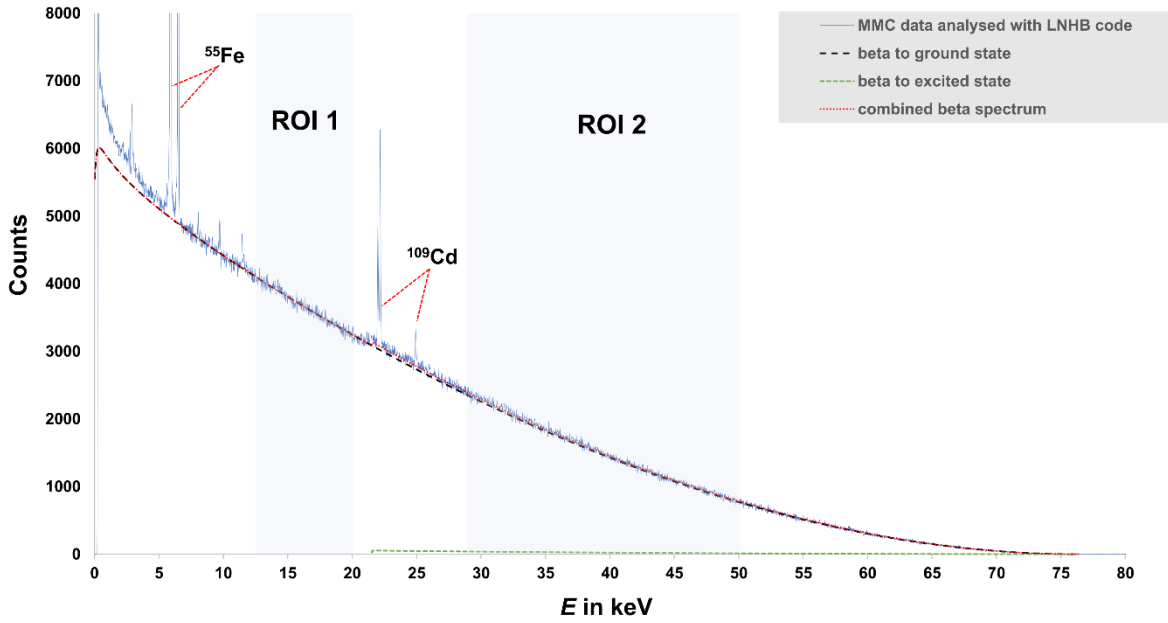


**Figure 9**

Measured MMC spectrum as shown in Figure 3 but after background subtraction. The two regions of interest (ROIs) were used to scale the computed beta spectra and to determine the transition probabilities of the two beta branches by means of two consecutive fit procedures. A corresponding residual plot is shown in Figure 10.

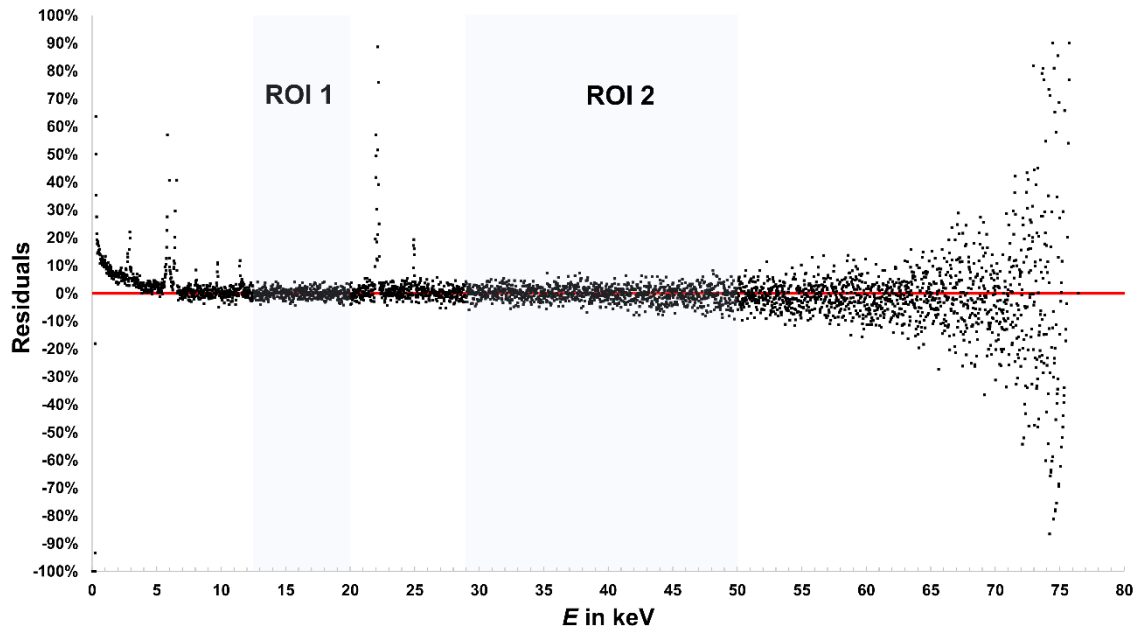


**Figure 10**

Residual plot using the data from Figure 9. The residuals are defined as  $(N_{i,\text{exp}} - N_{i,\text{theo}}) / N_{i,\text{theo}}$  with  $N_{i,\text{theo}}$  being the sum of computed beta spectra for both branches using the probabilities from the fit procedure and  $N_{i,\text{exp}}$  being the experimental data in bin  $i$ .